



Enhancement of voltammetric properties of silver nanoparticles doped ZnO nanorods for glucose biosensing

Asaad S. Yasir¹, Ammar S. Hameed¹, Noor J. Ridha^{1,*} , Firas K. Mohamad Alosfur², Khawla J. Tahir¹, and Rajaa A. Madlol¹

¹Department of Physics, College of Science, University of Kerbala, Kerbala, Iraq

²Department of Medical Physics, College of Applied Medical Sciences, University of Kerbala, Kerbala, Iraq

Received: 17 August 2022

Accepted: 28 November 2022

Published online:
31 January 2023

© The Author(s), under exclusive licence to Springer Science+Business Media, LLC, part of Springer Nature 2023

ABSTRACT

In this work, Ag nanoparticles (NPs) doped zinc oxide (ZnO) nanorods (NRs) have been prepared using hydrothermal method to be used as glucose biosensor. The preparation method includes three steps, seed, growth and coating. The first step was to coat the substrate with seed layer in which three samples were prepared using dip coating system with various number of dipping cycles (1, 2 and 3). The second step was to growth ZnO NRs. Finally, Ag NPs were coated on the ZnO NRs. Investigations such as structural properties, surface morphologies, optical properties and electrical resistance were conducted to determine the effects of doping the ZnO NRs with Ag NPs on these properties. As well as, the catalytic properties of glucose oxidase (GOx) and the functionality of the glucose sensor were taking place. The XRD results showed that the prepared samples have good crystallinity and high purity. The FESEM micrographs proved that the samples exhibited nanorods structures with varied thickness which increased by increasing the dipping cycles. The UV-Vis spectroscopy and electrical properties show that the prepared films were transparent with reduced energy gap and surface resistance by increasing the thickness due to the doping with Ag NPs. The results show that the cyclic voltammetry properties were improved by doping the ZnO NRs with 2% of Ag NPs. The scanning rate was 50 mV s^{-1} and the voltage range was $(-1.00 \text{ to } 1.00 \text{ V})$, and the concentration of glucose was from 0 to $500 \mu\text{M}$. The investigations proved that the sensitivity of the sensor was about $(350.1 \mu\text{A mM}^{-1} \text{ cm}^{-2})$, the detection limit was $(38.1 \mu\text{M})$ and the response time was (7 s). As well, a linear increment of current was noticed toward a varied range of glucose concentrations. Thus, the prepared electrode can be used in biosensors and transparent conductive electrodes (TCE) applications.

Address correspondence to E-mail: noor.jawad@uokerbala.edu.iq

1 Introduction

Diabetes affects the nature of patients' lives, their daily lives and their relationships with their families. Using an ordinary device to check the level of blood sugar—more than three times a day—by pricking the patients' fingers is a painful process. Therefore, scientists invented biosensor to facilitate these process since 1962 [1]. Then, sensors have continued developing to be robust, cheap, simple, highly sensitive, highly selective, responsive, and have high thermal stability [2].

One of the effective methods for identifying a particular type of molecules is the electrochemical sensing approach, due to its fast response and high sensitivity [3]. Electrochemical sensing devices based on cyclic voltammetry approach are one of the most widely used techniques for detection of environmental [4], food [5], pharmaceutical [6], clinical and biological compounds [7], due to electrical activity and the sensitive and selective identification [8]. Electrochemical biosensors are manufactured using chemically modified electrodes (CME), which are made by fusing conductive nanoparticles or redox mediators on the surface of solid electrodes [9]. This is because that nanomaterials have the potential rule to improve voltammetric analysis and electrochemical query by enhancing and improving the electrical conductivity of the modified electrodes [10].

Since the discovery of NPs, investigations on metals and metal oxides NPs have been conducted to be used in various chemical and biochemical reactions as a catalyst [11]. Zinc oxide (ZnO) is excellent nanomaterials with binding energy of exciton (60 MeV) and wide band gap (3.37 eV) that can be applied as working electrode [12]. Moreover, ZnO is promising candidate to be used as biosensors due to its repeatability and stability, [13]. When ZnO thin film irradiated by electromagnetic waves, excitons will be produced which enhance the polarization of the system. In addition, the polarization and optical absorption of ZnO thin film could be increased by increasing the annealing temperature due to the formation of a cone-like shape [14]. Hence, it was established that the polarization and optical absorption may also effected by oxygen vacancies [15].

Various morphologies of ZnO nanostructures such as nanorod structures, nanotubes or nanodisks could be applied as working electrode of biosensor to obtain larger surface area and greater stability of the enzyme [16, 17]. Nevertheless, pure ZnO has a limitation in the

transferability of electrons since the electrons returned back to the oxidation centers in the enzyme rather than moving to the working electrode in the biosensor which reduce the performance of biosensor [18]. Recently, researchers are focused on enhancing the catalytic behavior or facilitating the electron transfer rate of the biosensor by modifying the sensing elements [19, 20]. Therefore, it is necessary to introduce novel nanoparticles to modify the properties of ZnO nanostructures. The modification of ZnO nanostructures is done either by depositing nanoparticles on the surface of ZnO or by doping NPs in the crystal structure of ZnO. These dopant NPs have a high catalytic ability, such as cobalt, nickel and platinum [21] or high conductivity such as Au, Al ... etc [22]. For instance, Anusha et al. placed Pt nanoparticles on ZnO non-porous structures and found that it improved the glucose sensor's catalytic activity and ability to transport electrons [21]. Chu et al. revealed that doping ZnO nanorods with Ni by hydrothermal method reduced the conductivity of ZnO nanorods while improving the catalytic character of GOx toward glucose [23]. Meanwhile, Ag NPs are preferred candidate due to its good chemical stability and high electrical conductivity, [24]. According to the literature, doping ZnO with Ag NPs slightly reduced the surface roughness and hydrophilicity of ZnO-Ag nanorods but noticeably improved their ability to transport electrons, which improves the catalytic properties of GOx [25]. Therefore, NPs have been used in potential applications such as medicines, drug delivery systems and home appliances. However, using Ag NPs in the medical fields has a limitation due to the toxic effect of high concentration [26]. Therefore, a small amount of Ag NPs may be considered as a safe material.

In this study, Ag NPs have been used as dopant materials in ZnONRs to improve the optical, electrical, and voltammetric properties to obtain a large surface area with an abundance of high electrons involved in electrical conduction in the manufacture of a glucose biosensor.

2 Experimental part

2.1 Preparation of Ag NPs doped ZnO nanorods

To prepare the working electrode in electrochemical cell, which represents the biosensor, the following

steps should be followed: first step was to prepare a seed layer by dipping an ITO substrate in a coating solution using dip coating system. The coating solution was prepared by dissolving (0.1 mM) Zinc acetate [Zn (CH₃CO₂)₂·2H₂O] in ethanol by hotplate magnetic stirrer for 30 min at 60 °C. Annealing process was applied at 300 °C for 60 min to enhance the crystallinity.

After preparing a seed layer, a growth process was applied. The growth solution was prepared by dissolving zinc nitrate hexahydrate [Zn (NO₃)₂·6H₂O] (99.998%) and hexamethylenetetramine (HMT) (C₆H₁₂N₄) (99%) (Sigma- Aldrich) separately in deionized water at a concentration of 50 mM for 30 min. After that, these two solutions were mixed together for 20 min to obtain a homogeneous solution. The substrate was vertically placed in a glass vessel in which the sample was facing the wall for 120 min in an electric furnace at a temperature of 90 °C. This process is repeated three times to obtain ZnO NRs with lengths up to micrometer. After that, the substrate was immersed in a silver nitrate solution with concentration of 1 mM by dip coating device.

2.2 Preparation glucose biosensor

To immobilize the enzyme on the electrode surface, 10 mg/mL of Glucose oxides (GOx) (Sigma-Aldrich) was dissolved in a phosphate buffered saline (PBS). The electrode surface was rinsed with PBS to prepare the hydrophilic surface. 5 μL of the enzyme solution was deposited on the surface of the electrode and was left for 120 min to dry at room temperature. Cross-linking procedure was carried out by adding of 5% Nafion (C₇HF₁₃O₅S·C₂F₄) (Sigma-Aldrich) and 2.5% glutaraldehyde (C₅H₈O₂) (Sigma-Aldrich) on the surface of the electrode and was left to dry at room temperature. In addition, 2 μL of Nafion was deposited on the electrode surface to avoid possible enzyme leakage and eliminate foreign interferences.

2.3 Sample characterization

XRD (SHEMADZU/Japan) was employed for characterizations in order to assess the thin films' structural characteristics. The Debye–Scherrer equation could be used to calculate the crystalline size of particles below 60 nm [27]. The average crystal size of

the samples was calculated from the XRD data using Scherrer equation:

$$D = kD\lambda/(\beta \cos \theta) \quad (1)$$

$$\delta = 1/D^2 \quad (2)$$

$$\varepsilon = \beta/(4 * \tan(\theta)) \quad (3)$$

where D is crystal size (nm), k is Scherrer constant (0.9), λ is the wave length for X-ray source (1.5406 nm), β is full width at half maximum (FWHM) (°), and θ is peak position (°), δ is dislocation density, and ε is micro-strain.

As well as, the morphology and microstructure of the samples were examined using field emission scanning electron microscopy (FE-SEM) (EBSI Instrument: ZEISS SIGMA VP /Germany). The transparency of the prepared samples was examined using a Samsung Galaxy A31 camera. The camera featured a 48-MP primary sensor, a 5-MP depth camera, an 8-MP detector with a wide-angle lens, and a 5-MP macro camera. Shimadzu UV-VIS Spectrophotometer (UV-1900i) was used to evaluate the optical properties of the thin films. The optical transmittance of the synthesized thin films was analyzed in order to assess the transparency of the generated samples. The absorption coefficient (α) was calculated from the absorption data from which the band gap was calculated [11]. After finding the absorption coefficient corresponding to the direct band gap of the samples, a curve between the photon energy ($h\nu$) and the $(\alpha h\nu)^2$ was plotted. Finally, from the tangent to this curve, the energy gap can be calculated. To know the dimensions of the prepared samples such as diameters and how they are distributed, the FESEM images were analyzed using the image j program. Then, a statistical analysis of these measurements was performed and plotted to find out the average diameter of each sample and the effect of the thickness of the seed layer on the dimensions of the prepared samples.

2.4 Electrochemical measurements

The Ag NPs doped ZnO NRs were utilized as an electrode for the GOx immobilization of the enzyme. The voltammetry measurements were performed using a (DY2300 Series Potentiostat/Bipotentiostat) Digi-ivy, Inc. Austin, Texas _USA, Model: DY2321, software version: DY2321X040A0227IR; DY2300, Revision 10.12.20. Line Frequency (Hz): 60.

Additionally, a platinum (Pt) wire and an Ag/AgCl were used as counter and reference electrodes, respectively, as shown in Fig. 1.

The cyclic voltammetry method was used with scan rates of 50 mVs^{-1} and potential ranges between (-1.00 to 1.00) V. All electrodes were compared according to the determined net current response based on glucose concentration at a constant voltage. The current value of the buffer solution without glucose was subtracted from the current value of the solution with glucose to obtain the net current value, denoted as μA . Operational stabilities were examined by employing each electrode 5 times in a glucose solution with a different concentration ranging from 0 to $100 \mu\text{M}$.

3 Results and discussion

3.1 Structural properties

The as-prepared sample was investigated by XRD in order to identify the prepared material, as shown in Fig. 2. The figure demonstrates that all the prepared samples were contained five main diffraction patterns related to ZnO and three main diffraction

patterns for Ag. Additionally, the figure reveals that all of the diffraction peaks are conspicuously crystalline, in which the peaks corresponding to miller indices (100), (002), (101), (102), and (103) planes. According to the XRD analysis, the prepared samples can be indexed to the hexagonal, P6₃mc, wurtzite hexagonal phase of ZnO (JCPDS 96-901-1663). Particularly, the strong peak (002) indicates the preferred orientation. As well, it could be noticed clearly that the samples contained extra peaks consist of the (111), (200), and (311) planes related to Ag Cubic structure that can be indexed to the cubic Pn-3m related to (JCPDS 01-072-0607). Due to the presence of a tiny amount (1:50) of Ag NPs, the Ag NPs doped ZnO NRs pattern showed low intensity peaks of Ag NPs. The lattice constants of ZnO are ($a = 0.325 \text{ nm}$) and ($c = 0.520 \text{ nm}$), whereas for Ag are ($a = c = 0.490 \text{ nm}$).

It is obvious that the (002) plane alignment is referred to as the strong domain peak at value 34.540° . The presence of this peak indicated that the prepared samples exhibited 1D nanostructure with c direction; hence, ZnO powder [28, 29] or porous ZnO nanostructures [30] show low intensity (002) plane. This unique peak (002) indicated the good quality and the high purity of the prepared samples.

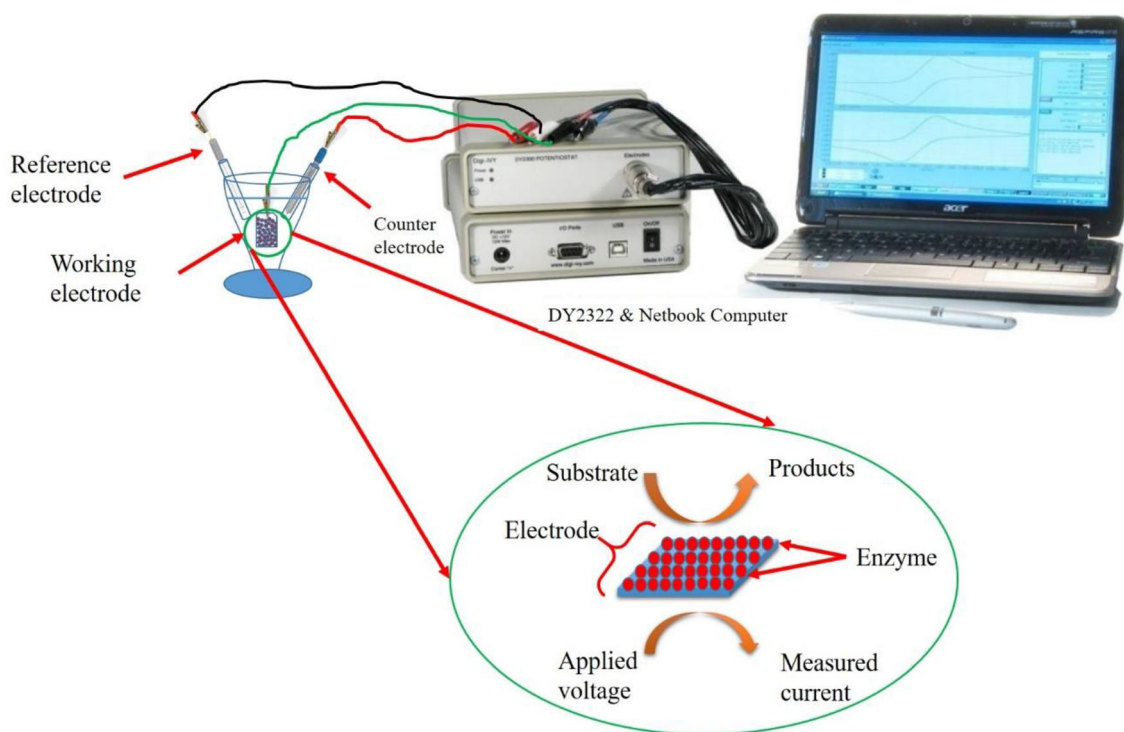


Fig. 1 Cyclic voltammetry system and mechanism of working electrode

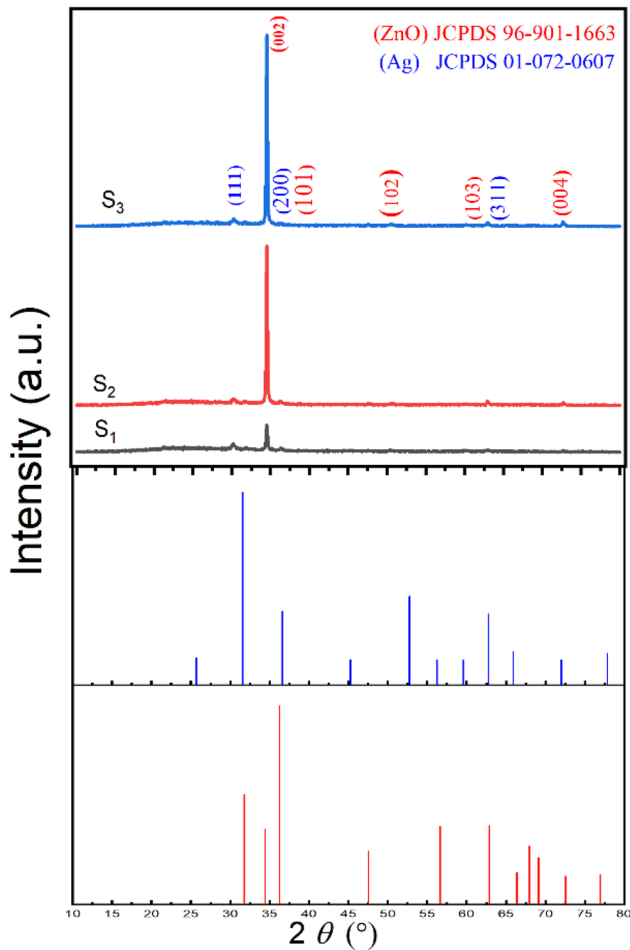


Fig. 2 XRD diffraction pattern for ZnO NRs doped Ag NPs compared with JPCDS cards

Using Scherrer Eq. (1), the crystals size of all samples was estimated. It was found that the sample S_1 has an average crystal size of about 25 nm, the sample S_2 is about 33 nm, and it is about 46 nm for the sample S_3 . It is obvious that the crystal size increased by increasing the dipping cycles as shown in Table 1.

By comparison, it could be noticed that the intensity of the peak at the ($2\theta = 34.540^\circ$) was low for sample S_1 (one dipping cycle). Meanwhile, by increasing the dipping times for sample S_2 (2 times dipping), the intensity was strongly increased. By further increment of dipping times sample S_3 (dipping cycles = 3 times), the highest intensity was detected. These results indicated that by increasing the number of coated layers, improvement of the structure was perceived.

Figure 3 represents the analysis of the structural properties of the samples using X'Pert program. By

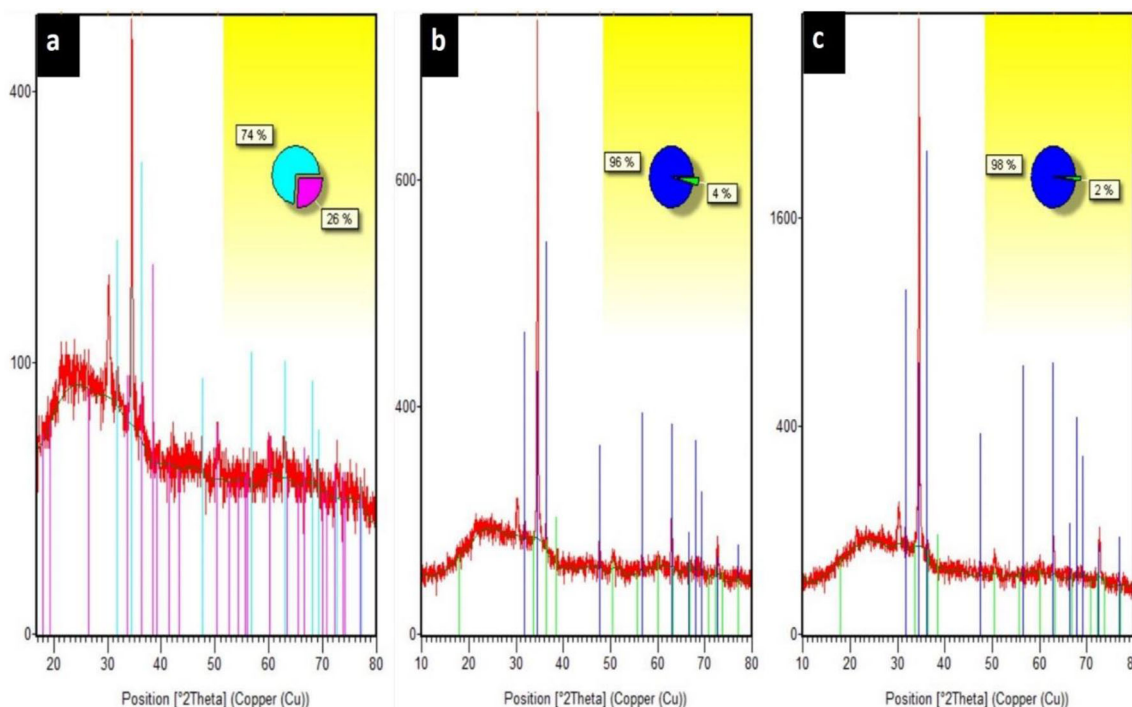
matching the data of XRD with the JPCDS, it was found that the ratio of Ag: ZnO were 26:74, 96:4 and 98:2 according to samples S_1 , S_2 and S_3 , respectively. These results indicated that as the number of dipping cycles increased, the ratio of Ag reduced.

ZnO NRs were grown on the top of different number of deposited ZnO seed layers. The surface morphology examination of the prepared ZnO electrodes was carried out by FESEM. Figure 4 shows the surface morphology, cross section, and size of NRS distributions. Fig. 4a, b and c represents the surface morphology of the samples S_1 , S_2 and S_3 , respectively. Generally, all the samples displayed small nanoparticles with average size around (25–45 nm). These nanoparticles agglomerated and stacked together to form larger hexagonal combined nanorods structures that were longitudinally aligned on the surface of the substrate. The ZnO NRs were grown with flat feature surfaces of size ranging around (100, 120 and 150) nm for the samples S_1 , S_2 and S_3 , respectively. As for images (4 d, e and f), they denoted a cross section of the samples S_1 , S_2 and S_3 , correspondingly. These images show the variations in the length of the nanorods for samples S_1 , S_2 and S_3 as 380 nm, 466 nm, and 708 nm, respectively. The difference between these samples is the number of seed layer, the larger the number of the seed layers, the greater the height of the nanorods. As well as, the diameter of the nanostructure increases due to its dependency on the size of the particles of the aggregate seed layer. By comparison, wider, longer and more upright nanorods can be created with a thicker seed layer. As well, the distance between adjacent nanorods shrunk as the seed layers became thicker until the substrate was completely filled. The images (g, h and i) illustrate the size of NRs distributions of the three samples (S_1 , S_2 and S_3), respectively. As the statistical results, the diameters of samples S_1 , S_2 and S_3 are (23.68, 27.5, and 33.95 nm), respectively. It can be noticed clearly that the higher the number of dipping cycles and thus thicker seed layer, the largest the diameter. Reasonable results were obtained by comparing the crystal size obtained from XRD with particles size obtained from the FESEM images. It could be noticed a small difference in sample S_3 between these results because they are approximate values and the clarity of the FESEM images does not give the exact results.

Figure 5 illustrates the EDX of the three samples S_1 , S_2 and S_3 , respectively. It is clear that the percentage

Table 1 Illustrate all parameters calculated from XRD data

Sample ID	2θ ($^\circ$)	β ($^\circ$)	D (nm)	Average crystal size (nm)	$\delta^* 10^{-3} (\text{nm})^{-2}$	$\varepsilon * 10^{-3}$
S ₁	30.166	0.394	21	25	2.289	6.373
	34.525	0.197	42		0.56	2.763
	36.318	0.472	18		3.192	6.283
	62.909	0.472	20		2.572	3.369
S ₂	34.518	0.157	53	33	0.358	2.211
	36.323	0.315	27		1.418	4.188
	47.684	0.472	18		2.957	4.663
	62.937	0.394	24		1.786	2.806
	72.686	0.236	42		0.573	1.401
S ₃	30.246	0.472	17	46	3.294	7.626
	34.519	0.157	53		0.358	2.211
	62.963	0.315	30		1.143	2.244
	72.618	0.118	83		0.144	0.701

**Fig. 3** ZnO and Ag ratio in the XRD analysis depending on (Ag—JCPDS 01-072-0607) and (ZnO—JCPDS 96-901-1663) where **a** sample S₁, **b** sample S₂ and **c** sample S₃

of the oxygen is low while the percentage of zinc is very high. This is evidence to the presences of oxygen vacancy. Whereas the silver does not appear in this test because of the presence of oxygen vacancies, silver did not appear on the surface, but rather concentrated in the interfacial spaces of the nanorods.

4 Growth mechanism

In this work, ZnO NRs were prepared using hydrothermal process and then coated with Ag NPs. This hydrothermal processing could be described as a heterogeneous reaction that occurs in aqueous systems under high temperature and pressure to dissolve and recrystallize the zinc nitrate which is generally insoluble under normal environments [31]. The structure of ZnO NRs is often significantly

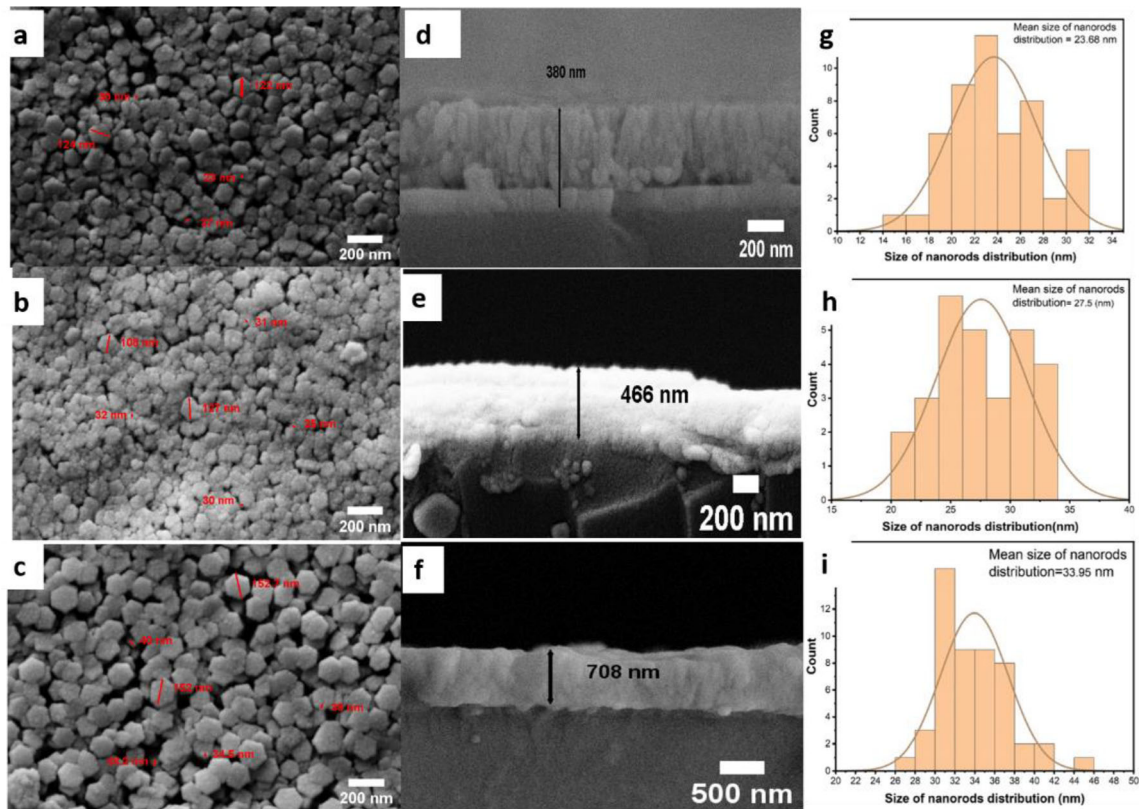


Fig. 4 Shows the surface morphology (a, b, and c), cross section (d, e, and f), size of NRs distributions (g, h, and i)

influenced by the seed layer [32], the growth solution type and concentrations [33], solvent type [34], growth duration and temperatures [35], and annealing temperature [36]. Specifically, researchers proposed that employing smaller seed particles can control the diameter, vertical alignment, and uniform growth of the nanorods [37]. As a result, efforts placed a lot of emphasis on producing small seed particles utilizing a low precursor concentration in recognition of the significance of seeds. Nevertheless, the thickness characterization of the films prepared by the dip coating system depends on several factors such as drawing velocity, temperature, number of dips, ambient humidity, and composition of the solution [38]. The substrate was immersed in the solution at a constant speed and left in the solution for a certain period in order to let the solution to be adhered on the substrate. A thin film begins to form when the substrate is withdrawn from the solution, so that the greater the speed, the thicker the thickness of the film [39, 40]. In addition, the thickness is affected by the viscosity of the solution and the surface tension [41]. Therefore, the thickness of the thin films formed by fluids is described by the classical

equation of Landau—Levich [42]. The number of the seed layers differentiates these samples, in which more seed layers produced thicker seed layer. As a result, this seed layer controls the growth process and thus the morphology of the ZnO nanorods. Due to the nanorods dependence on the seed layers, it grew taller and had a larger diameter on the thicker and aggregated particle size. In addition, when the seed layer got thicker, the space between adjacent nanorods got smaller and the substrate was fully filled with ZnO NRs.

4.1 Optical properties

The prepared Ag NPs doped ZnO NRs show high transparency, as shown in Fig. 6. The optical measurements of the Ag NPs doped ZnO NRs were made using a Shimadzu UV-VIS 1900i Spectrophotometer with a 190–1100 nm wavelength range at room temperature as shown in Fig. 7. The results showed high transmittance in the visible to near-infrared range of all samples with some variation in values due to the number of dipping cycles. The transmittance increases sharply in the wavelength region of 300 nm,

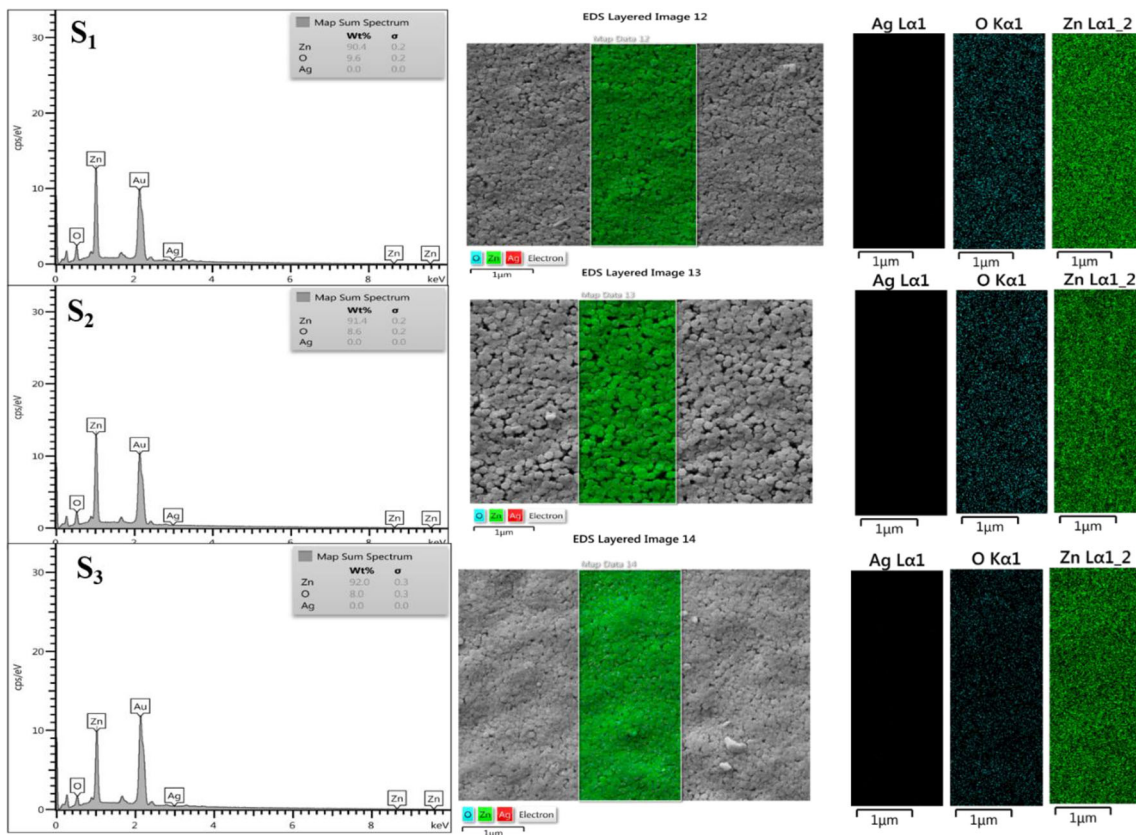


Fig. 5 Mapping and EDS for Ag NPs doped ZnO NRs for samples S₁, S₂ and S₃

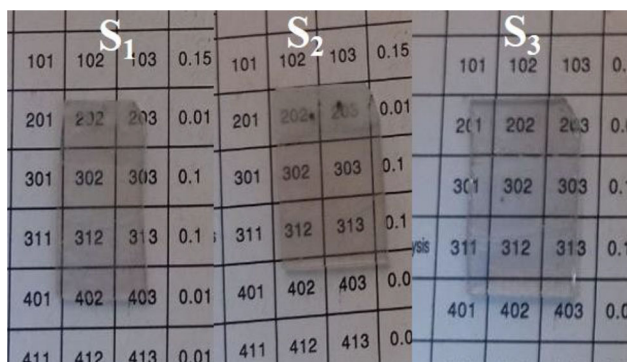


Fig. 6 Ag NPs doped ZnO NRs samples transparency

where it reaches 70%, and value rises to 80%. Nevertheless, the higher the number of layers (and thus longer nanorods), the lower the optical transmittance.

The optical characterization of thin films provides the information about physical properties such as bandgap energy, band formation and optically active defects. The optical transmittance and energy gap values are affected by the thickness of the film as the transmittance decreases sharply in the ultraviolet region due to the high absorption in the energy gap.

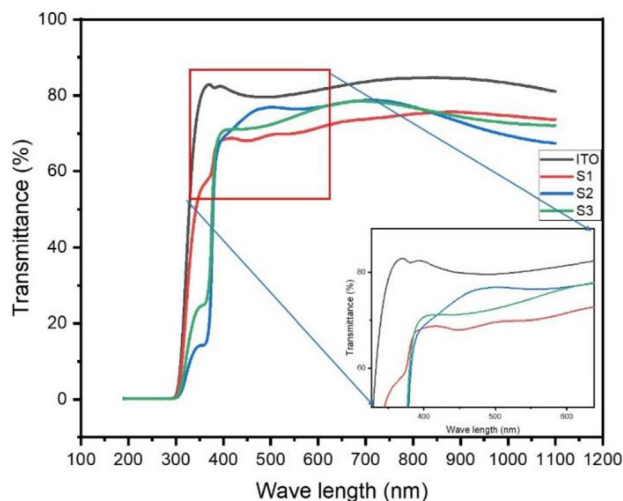


Fig. 7 Optical properties for Ag NPs doped ZnO NRs

As expected, the transmittance decreases with increasing thickness of the film because many more photons are absorbed into the material by increasing thickness. In addition, a sharp transmittance edges appeared in all the samples that showed a red shift toward the lower energies and larger wavelength.

This red shift proportion directly to the length of the nanorods.

The energy gap is calculated from the data produced by measuring the optical properties. After knowing the values of transmittance, absorbance and absorption coefficient and knowing the thickness of the thin film (through FESEM examination), a graphic relationship can be drawn between the energy ($E = hv = (1240/\lambda)$ eV) and $(\alpha hv)^2$ (eV/cm)² of direct transition semiconductors. By taking the tangent to this curve, we find the energy gap for each of the three samples. As shown in Fig. 8, it is clear that the energy gap decreases with increasing the number of coating layers of the sample; in other words, the energy gap decreases with increasing thickness of the thin film. In addition, the energy gap decreases when doping with Ag NPs.

4.2 Electrical properties

Figure 9 shows the electrical properties of Ag NPs doped ZnO NRs. The linear relationship suggests that all of the ZnO thinfilms doped with Ag NPs have an Ohmic characteristic. Generally, the results show that sample S₃ exhibited the best conduction; it was found that the electrical properties improved by increasing of the thickness, growing the diameters of nanorods and doping with Ag NPs. This result caused by the nature of the nanorods structure which controls the path of electrons in a specific direction, so the conduction speed increases, which gives a positive indication of the decrease in the resistance of the thin film. As well, the doping with Ag NPs improves the electrical conductivity due to the abundance of electrons in which they participate in the thin film’s conduction. Table 2 illustrates

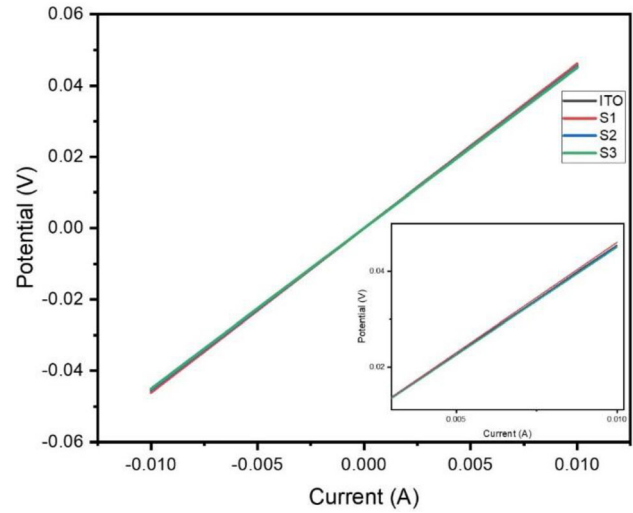


Fig. 9 I–V properties for Ag NPs doped ZnO NRs thin films

decreasing resistance values with increasing the number of seed layers.

4.3 Cyclic voltammetry properties

Cyclic voltammetry measurements were made in the absence and presence of glucose using the manufactured electrode (Ag NPs doped ZnO NRs) as a working electrode, the reference electrode is (Ag/AgCl) and the auxiliary electrode is (Pt electrode). These electrodes were used as the basis of the interaction between the enzyme and glucose. The scanning rate was 50 mV s⁻¹, and the voltage range was (– 1.00 to 1.00 V). The concentration difference of glucose was studied for the three samples with a difference in the number of seed layers. The enzyme was coated on the prepared electrode electrochemically, where its properties are described by cyclic

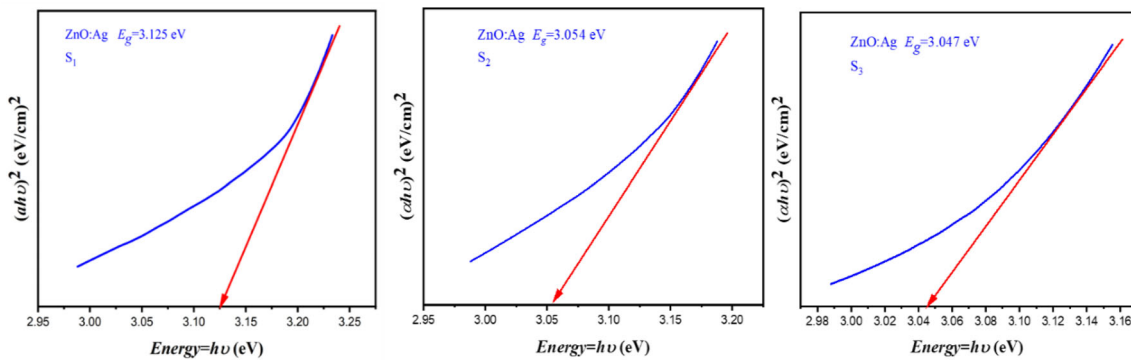
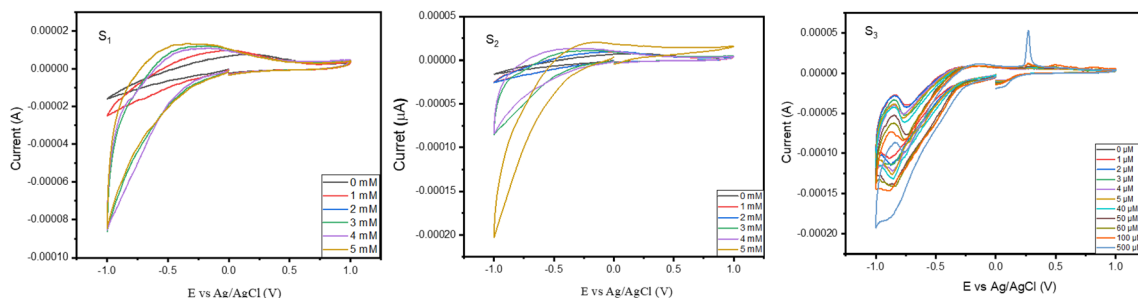
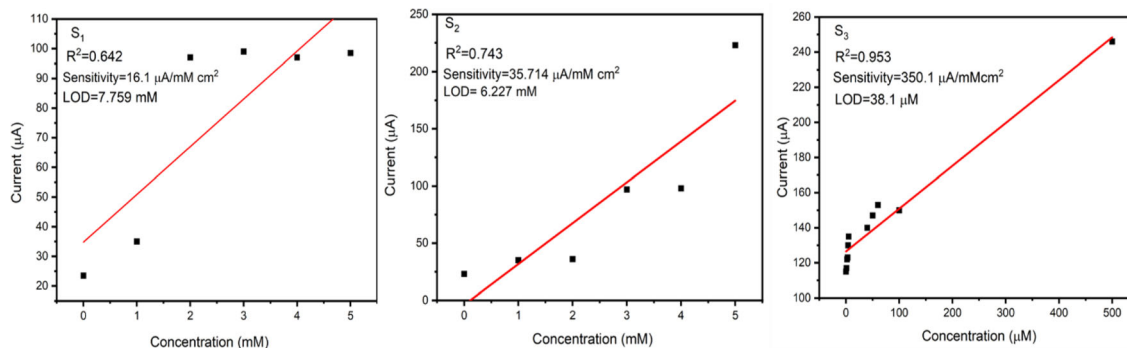


Fig. 8 Energy gap for Ag NPs doped ZnO NRs (S₁) 1 seed layer (S₂) 2 seed layer (S₃) 3 seed layer

Table 2 FPP method sheet resistance for samples of varying dipping cycles

Sample ID	Dipping cycles	Nanostructures	Resistance R_s (Ω)	Sheet resistance R_{ss} (Ωsq^{-1})
ITO	0	–	4.583	18.372
S ₁	1	NRs + Ag NPs	4.609	18.476
S ₂	2	NRs + Ag NPs	4.535	18.182
S ₃	3	NRs + Ag NPs	4.505	18.060

**Fig. 10** Cyclic voltammograms. The Ag NPs doped ZnO NRs in the presence of glucose in 0.1 M PBS with a scan rate of 50 mV s^{-1} (S₁) 1 seed layer, (S₂) 2 seed layers, and (S₃) 3 seed layers**Fig. 11** The Ag NPs doped ZnO NRs calibration curves between measured current and different concentrations

voltammetry in phosphate buffer saline (PBS) solution. This medium is one of the best options for studying the electrochemical enzymatic reaction. Figure 10 shows the increment of the area in the plot with the increase in the number of coating layers for the samples in which the reaction takes place in terms of oxidation and reduction. The lower the percentage of doping with Ag NPs, the better the performance of the manufactured electrode. Sample S₃ shows a lower detection limit compared to other two samples due to the higher surface area and lower Ag percentage, as mentioned previously. Figure 11 shows the relation between the increments of current as a function of glucose concentration. The calibration curve was plotted by the OriginLab program as illustrate in the figure. The optimum sample S₃ showed that the limit of detection (LOD), the sensitivity, the response time,

and linearity (R [2]) were ($38.1 \mu\text{M}$), ($350.1 \mu\text{A mM}^{-1} \text{cm}^{-2}$) (7 s) (0.953), respectively. These results indicated that the reaction improved and the detection limit decreased by increasing the thickness of the films. In addition, these results showed a detection limit less than [43] and a sensitivity of higher than [23, 44].

5 Conclusion

There are potential applications of Ag NPs in nano-electronics, medicines, and home appliances. In this work, Ag NPs were coated the ZnO NRs using the dip coating system to be used as glucose biosensor. The electrochemical behavior of the prepared electrode toward glucose oxidation was studied, and the

effective attraction to the enzyme by glucose was demonstrated. The results obtained from the reaction showed that it is possible to provide a beneficial microenvironment for the enzyme and to promote glucose oxidation. In addition, it is important for detection the glucose in biological systems. The manufactured electrode can be used as a glucose sensor in liquids containing human serum, since the active medium is similar in its properties to human blood.

Author contributions

The presented plan was proposed by NJR and ASY. The experimental work, calculations and theoretical development were done by ASY. The analytical techniques were confirmed by ASY and ASH. Each one of the authors contributed to the final manuscript by continuous discussions on the findings and giving the solutions and suggestion to obtain the final conclusion.

Funding

This research was entirely self-funded.

Data availability

This published article [and its additional information files] contain all data produced or analyzed during this investigation.

Declarations

Conflict of interest The authors declare that there are no competing interests with regard to the publication of this work.

References

1. L.C. Clark Jr., *Ann. NY Acad. Sci.* **102**, 29 (1962)
2. K.K. Swain, S. Bhand, *Anal. Bioanal. Chem.* **413**, 1715 (2021)
3. J. Lu, I. Do, L.T. Drzal, R.M. Worden, I. Lee, *ACS Nano* **2008**, 2 (1825). <https://doi.org/10.1021/nn800244k>
4. B. Podola, E.C.M. Nowack, M. Melkonian, *Biosens. Bioelectron.* **19**, 1253 (2004)
5. H. Yang, L. Qu, Y. Lin, X. Jiang, Y.-P. Sun, *J. Biomed. Nanotechnol.* **3**, 131 (2007)
6. E. Helmerhorst, D.J. Chandler, M. Nussio, C.D. Mamotte, *Clin. Biochem. Rev.* **33**, 161 (2012)
7. E.B. Bahadır, M.K. Sezginçtürk, *Anal. Biochem.* **478**, 107 (2015). <https://doi.org/10.1016/j.ab.2015.03.011>
8. V.K. Gupta, M.L. Yola, N. Atar, A.O. Solak, L. Uzun, Üstündağ, *Z. Electrochim. Acta* **105**, 149 (2013)
9. H. Karimi-Maleh, P. Biparva, M. Hatami, *Biosens. Bioelectron.* **48**, 270 (2013)
10. N. Atar, T. Eren, M.L. Yola, *Thin Solid Films* **590**, 156 (2015)
11. K.M.M. Abou El-Nour, A. Eftaiha, A. Al-Warthan, R.A.A. Ammar, *Arab. J. Chem.* **3**, 135 (2010)
12. W. Guo, T. Liu, H. Zhang, R. Sun, Y. Chen, W. Zeng, Z. Wang, *Sensors Actuators B Chem.* **166–167**, 492 (2012). <https://doi.org/10.1016/j.snb.2012.02.093>
13. M.H. Asif, A. Razaq, N. Akbar, B. Danielsson, I. Sultana, *Mater. Res. Express* **6**, 95028 (2019). <https://doi.org/10.1088/2053-1591/ab2d4c>
14. R. Kurniawan, F. Willy, E. Nurfani, S. Muhammadiyah, I.M. Sutjahja, T. Winata, Y. Darma, *Mater. Res. Express* **4**, 24003 (2017)
15. N. Mufti, S. Maryam, A.A. Fibriyanti, R. Kurniawan, A. Fuad, A. Taufiq, *Scanning* **2018**, 6545803 (2018). <https://doi.org/10.1155/2018/6545803>
16. R. Ahmad, N. Tripathy, J.H. Kim, Y.-B. Hahn, *Sens. Actuators B Chem.* **174**, 195 (2012). <https://doi.org/10.1016/j.snb.2012.08.011>
17. K. Yang, G.-W. She, H. Wang, X.-M. Ou, X.-H. Zhang, C.-S. Lee, S.-T. Lee, *J. Phys. Chem. C* **113**, 20169 (2009)
18. Q. Mao, W. Jing, W. Gao, Z. Wei, B. Tian, M. Liu, W. Ren, Z. Jiang, *Micromachines* **12**, 977 (2021)
19. K. Tian, S. Alex, G. Siegel, *Engineering* **46**, 548 (2015)
20. L. Fang, B. Liu, L. Liu, Y. Li, K. Huang, Q. Zhang, *Chemical* **222**, 1096 (2016)
21. J.R. Anusha, H.-J. Kim, A.T. Fleming, S.J. Das, K.-H. Yu, B.C. Kim, C.J. Raj, *Sensors Actuators B Chem.* **202**, 827 (2014)
22. Y. Wei, Y. Li, X. Liu, Y. Xian, G. Shi, L. Jin, *Biosens. Bioelectron.* **26**, 275 (2010). <https://doi.org/10.1016/j.bios.2010.06.006>
23. X. Chu, X. Zhu, Y. Dong, T. Chen, M. Ye, W. Sun, *J. Electroanal. Chem.* **676**, 20 (2012)
24. S.S. Patil, M.G. Mali, M.S. Tamboli, D.R. Patil, M.V. Kulkarni, H. Yoon, H. Kim, S.S. Al-Deyab, S.S. Yoon, S.S. Kolekar, *Catal. Today* **260**, 126 (2016)
25. F. Zhou, W. Jing, P. Liu, D. Han, Z. Jiang, Z. Wei, *Sensors* (2017). <https://doi.org/10.3390/s17102214>

26. P.V. AshaRani, G. Low Kah Mun, M.P. Hande, S. Valiyaveetil, *ACS Nano* **3**, 279 (2009)
27. L. Gelisio, P. Scardi, *Acta Crystallogr. Sect. A Found. Adv.* **72**, 608 (2016)
28. H.B.A. Kadhim, N.J. Ridha, F.K.M. Alosfur, N.M. Umran, R. Madlol, K.J. Tahir, R.T. Ahmed, *J. Phys.: Conf. Ser.* **1**, 1 (2018)
29. N.J. Ridha, F.K.M. Alosfur, H.B.A. Kadhim, L.H. Aboud, N. Al-Dahan, *J. Mater. Sci. Mater. Electron.* **31**, 9835 (2020)
30. N.J. Ridha, A.A. Umar, F. Alosfur, M.H.H. Jumali, M.M. Salleh, *J. Nanosci. Nanotechnol.* **13**, 2667 (2013)
31. S. Asavapisit, G. Fowler, C.R. Cheeseman, *Cem. Concr. Res.* **27**, 1249 (1997)
32. J. Castillo-Rodriguez, C.J. Pereyra, P. Valente, A. Seré, R.E. Marotti, S.A. Hevia, E.A. Dalchiale, R. del Rio Quero, *J. Solid State Electrochem.* **24**, 797 (2020)
33. Y.F. Hsu, Y.Y. Xi, K.H. Tam, A.B. Djurišić, J. Luo, C.C. Ling, C.K. Cheung, A.M.C. Ng, W.K. Chan, X. Deng, *Adv. Funct. Mater.* **18**, 1020 (2008)
34. S.M. Saleh, A.M. Soliman, M.A. Sharaf, V. Kale, B. Gadgil, *J. Environ. Chem. Eng.* **5**, 1219 (2017)
35. K.A. Wahid, W.Y. Lee, H.W. Lee, A.S. Teh, D.C.S. Bien, I. Abd Azid, *Appl. Surf. Sci.* **283**, 629 (2013)
36. Z.B. Fang, Z.J. Yan, Y.S. Tan, X.Q. Liu, Y.Y. Wang, *Appl. Surf. Sci.* **241**, 303 (2005)
37. Y. Tak, K. Yong, *J. Phys. Chem. B* **109**, 19263 (2005)
38. D. Lončarević, Ž Čupić, *Industrial Applications of Nanomaterials* (Elsevier, Amsterdam, 2019)
39. Y. Tong, S. Bohm, M. Song, J. Austin, *Nanomed. Nanotechnol.* **1**, 1003 (2013)
40. K.L. Choy, *Prog. Mater. Sci.* **48**, 57 (2003). [https://doi.org/10.1016/S0079-6425\(01\)00009-3](https://doi.org/10.1016/S0079-6425(01)00009-3)
41. C.J. Brinker, A.J. Hurd, P.R. Schunk, G.C. Frye, C.S. Ashley, *J. Non Cryst. Solids* **147–148**, 424 (1992). [https://doi.org/10.1016/S0022-3093\(05\)80653-2](https://doi.org/10.1016/S0022-3093(05)80653-2)
42. L. Landau, B. Levich, *Dynamics of curved fronts* (Elsevier, Amsterdam, 1988)
43. V. Fidal, S. Inguva, S. Krishnamurthy, E. Marsili, J.-P. Mosnier, T.S. Chandra, *Enzyme Microb. Technol.* **96**, 67 (2017)
44. Z.W. Zhao, X.J. Chen, B.K. Tay, J.S. Chen, Z.J. Han, K.A. Khor, *Biosens. Bioelectron.* **23**, 135 (2007)

Publisher's Note Springer Nature remains neutral with regard to jurisdictional claims in published maps and institutional affiliations.

Springer Nature or its licensor (e.g. a society or other partner) holds exclusive rights to this article under a publishing agreement with the author(s) or other rightsholder(s); author self-archiving of the accepted manuscript version of this article is solely governed by the terms of such publishing agreement and applicable law.